# Characterization of Microstructure in Laser-Surface-Alloyed Layers of Aluminum on Nickel

S. BYSAKH, S.K. MITRA, G. PHANIKUMAR, J. MAZUMDER, P. DUTTA, and K. CHATTOPADHYAY

In order to obtain basic understanding of microstructure evolution in laser-surface-alloyed layers, aluminum was surface alloyed on a pure nickel substrate using a $CO_2$ laser. By varying the laser scanning speed, the composition of the surface layers can be systematically varied. The Ni content in the layer increases with increase in scanning speed. Detailed cross-sectional transmission electron microscopic study reveals complexities in solidification behavior with increased nickel content. It is shown that ordered B2 phase forms over a wide range of composition with subsequent precipitation of $Ni_2Al$, an ordered $\omega$ phase in the B2 matrix, during solid-state cooling. For nickel-rich alloys associated with higher laser scan speed, the fcc $\gamma$ phase is invariably the first phase to grow from the liquid with solute trapping. The phase reorders in the solid state to yield $\gamma'$ $Ni_3Al$. The phase competes with $\beta$ AlNi, which forms massively from the liquid. The $\beta$ AlNi transforms martensitically to a 3R structure during cooling in solid state. The results can be rationalized in terms of a metastable phase diagram proposed earlier. However, the results are at variance with earlier studies of laser processing of nickel-rich alloys.

## I. INTRODUCTION

LASER surface alloying is a novel technique of applying desired protective coatings on engineering components using the intense power of a laser. It is capable of producing a thin surface layer on a substrate alloyed with the desired element. The details of laser surface modification are reviewed elsewhere.[1] Through proper control and optimization of the various experimental parameters such as laser power, spot size, laser scan speed, and feed rate of the alloying powder, an alloyed layer of the desired composition and improved surface properties can be achieved on to the workpiece.[2,3,4] Laser surface alloying is increasingly becoming an important industrial tool for surface modification to impart additional functionality in actual use. In order to achieve this goal, one needs to employ rational alloy design criteria to obtain the required chemistry and the microstructure within the alloyed layer. The understanding of the microstructure evolution in the alloyed surfaces as a function of processing parameters and chemistry is, therefore, crucial.

Nickel aluminides are well known for exhibiting interesting properties such as high strength and corrosion/oxidation resistance at elevated temperatures. Since laser surface alloying is capable of producing fine as well as metastable microstructures, several investigators have explored this technique for synthesizing surface layers of nickel aluminides using preplaced alloy powders.[5,6] In the present article, we report the results of an extensive investigation on the microstructure and phase evolution during surface alloying of aluminum on pure nickel substrate. We attempt to rationalize our observations in terms of phase transformation under nonequilibrium conditions generated by the process of laser melting and subsequent rapid solidification.

## II. EXPERIMENTAL

A 5.4 kW CW $CO_2$ laser (TRUMF made) was used for the surface alloying of nickel with aluminum. For cladding, a beam size of 2-mm diameter in mixed mode was used. The substrate dimensions were $10 \times 30 \times 100$ mm. The laser beam created a molten pool on the pure nickel substrate in which aluminum powder was added as an alloying element. The powder was gravity fed using a controlled flow of He for smooth feeding and fluidizing the powder. A shroud of argon gas was used for preventing oxidation during alloying. Alloying was carried out with a constant power of 2.7 kW and powder feed rates of 3.2 and 6.4 gm/min. The detailed investigation was carried out on samples obtained with a feed rate of 3.2 g/min. Laser scan speed was chosen as the variable parameter. Different scan rates ranging from 4.2 to 51 mm/s were used. Experiments were carried out with single pass and multiple passes of the laser beam with a clad-layer overlap of about 0.5 mm of the adjacent clad edges. The width of the laser-clad layer thus produced by each single pass was about 2.5 mm. The alloyed tracks were characterized by X-ray diffraction, optical microscopy, and EDX analysis in a JEOL* JSM 840A scanning electron microscope (SEM).

*JEOL is a trademark of Japan Electron Optics Ltd., Tokyo.

Detailed transmission electron microscopy (TEM) was carried out using cross-sectional specimens prepared from samples

S. BYSAKH, Visiting Scientist, is with the Nanocharacterization Research Group, Nanomaterials Laboratory (NML), National Institute for Materials Science (NIMS), Ibaraki–305003, Japan. S.K. MITRA, Programmer Analyst, Syntel(I) Limited, Chennai–600 015, India. G. PHANIKUMAR, Visiting Scientist, is with the Institut fur Raumsimulation, Deutsches Zentrum fur Luft- und Raumfahrt e.V., D-51170 Koln, Germany. J. MAZUMDER, Professor, is with the Department of Mechanical Engineering, University of Michigan, Ann Arbor, MI 48106. P. DUTTA, Associate Professor, Department of Mechanical Engineering, and K. CHATTOPADHYAY, Professor, Department of Metallurgy, are with the Indian Institute of Science, Bangalore–560 012, India. Contact e-mail: kamanio@metalrg.iisc.ernet.in or chairman@mrc.iisc.ernet.in

Manuscript submitted March 1, 2002.



Reproduced with permission of the copyright owner. Further reproduction prohibited without permission.

processed with single pass. The goal was to investigate the finer details of the microstructure that evolved during rapid solidification processing and identify the different phases formed at various scan speeds. A JEOL* JEM 2000FX II transmission electron microscope was used for this purpose.

*JEOL is a trademark of Japan Electron Optics Ltd., Tokyo.

## III. RESULTS

### A. *Morphology and Composition of Laser Clad*

Figure 1 shows a typical morphology of the transverse section of a surface-alloyed layer obtained with a single pass of laser with a scan speed of 51 mm/s. With decreasing scan speed, the depth of the alloyed zone increases. The depth varied from 120 $\mu$m for 51 mm/s scan speed to 1300 $\mu$m for a scan speed of 4.2 mm/s. The composition profiles indicate rapid rise of aluminum concentration near the melt substrate interface followed by a region of uniform average concentration (Figure 2(a)). The aluminum content sometimes increases close to the top surface. The average compositions of the pools in the flat regions as a function of scan rates at two constant feed rates are shown in Figure 2(b). The alloy compositions increasingly become aluminum rich with decreasing scan speed. This indicates that the expected higher melt depth of the nickel substrate (due to its characteristic good optical absorption property) is more than compensated by the higher melting rate and alloying of aluminum powder at lower scan rates. Although the nature of the curve remains the same, it can be seen that an increase in the feed rate shifts the compositions to higher level of aluminum concentration. Thus, for maintaining a given clad composition, higher feed rate demands a higher scan speed. Thus, for equivalent surface-alloyed layer composition, the microstructure obtained for the case of higher feed rate will represent a more rapid solidification. However, this aspect will not be discussed further in this article. For the rest of the article, all the results that will be presented correspond to the feed rate of 3.2 g/min. Figure 3 shows the X-ray diffractrograms of the alloy surfaces at different scan speeds. The phases corresponding to the observed peaks are marked. All the diffractograms contain small peaks of aluminum corresponding to a small amount of unmixed aluminum near the top surface, in addition to peaks from the nickel substrate. Additionally, some weak peaks corresponding to $Al_2O_3$ can be seen at low scan rates. The predominant phase at low scan rate is $Al_3Ni$. With increasing scan rate, bcc NiAl phase appears followed by $Ni_3Al$, consistent with the trend in the alloy composition. The microstructure evolution in the alloyed layers was followed *via* detailed TEM of cross-sectioned samples. The results are elaborated in Sections B–1 through 4.

### B. *Microstructure Analysis*

#### 1. *Surface alloying at a scan rate of 4.2 mm/s (average composition $Al_{70}Ni_{30}$)*

The total depth of the alloyed layer under this processing condition is ~1300 $\mu$m. Primarily dendritic microstructure can be seen near the top of the surface layer. A typical bright-field micrograph from a layer near the top of the surface (~1200 $\mu$m from the substrate) is shown in Figure 4(a). Systematic tilting to orient the grain along major zone axes lying on the unit stereographic triangle established the phase to be $Al_3Ni$. This is also shown in Figure 4(a). The interdendritic region contains fine polycrystals (Figure 4(b)(i)), which yield diffraction rings (Figure 4(b)(ii)). The rings can be indexed in terms of coexisting $\alpha$-Al and $Al_3Ni$ phases. The microstructure of the pool at a distance of 900 $\mu$m from the substrate is shown in Figures 5(a) and (b). It again predominantly consists of dendrites of $Al_3Ni$ (the SADP in the insets). However, interdendritic regions are larger and exhibit a eutectic morphology. Selected area diffraction patterns conclusively establish the continuous phase in the interdendritic region to be $\alpha$ Al, while the embedded eutectic second-phase particles are $Al_3Ni$ (the diffraction pattern in the inset). Figure 5(c) shows the eutectic regions, which are more prominent in the middle of the alloyed pool (700 $\mu$m from the substrate). To sum up, the sample primarily contains fine $Al_3Ni$ dendrites with $\alpha$ Al/$Al_3Ni$ eutectic in the interdendritic regions.

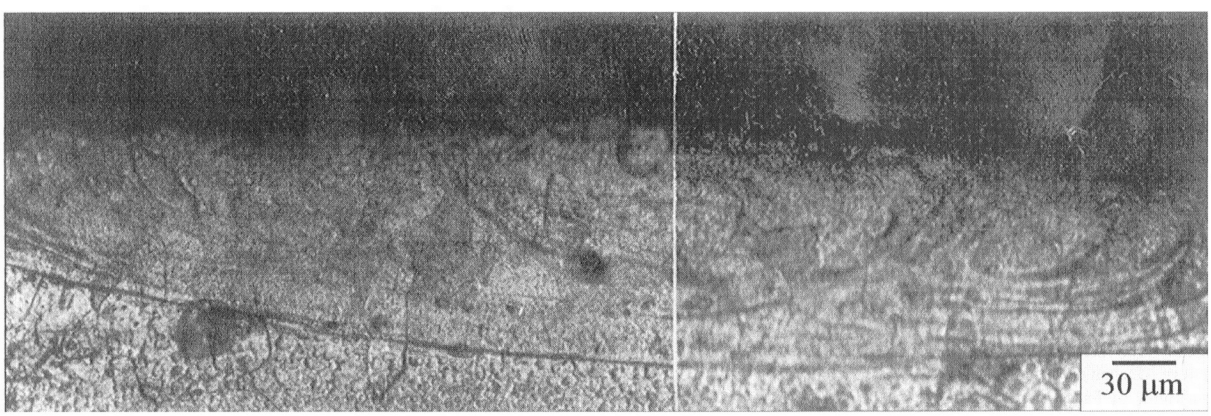


Fig. 1—Optical micrograph revealing the cross-section morphology of the laser-alloyed pool processed at a scan rate of 51 mm/s.



Reproduced with permission of the copyright owner. Further reproduction prohibited without permission.

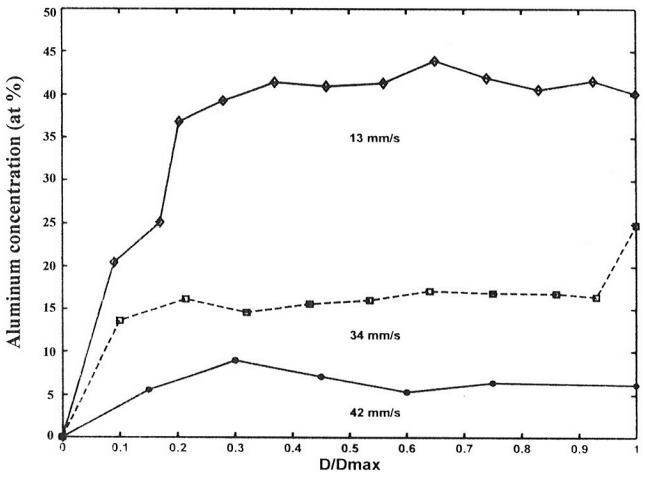


(*a*)

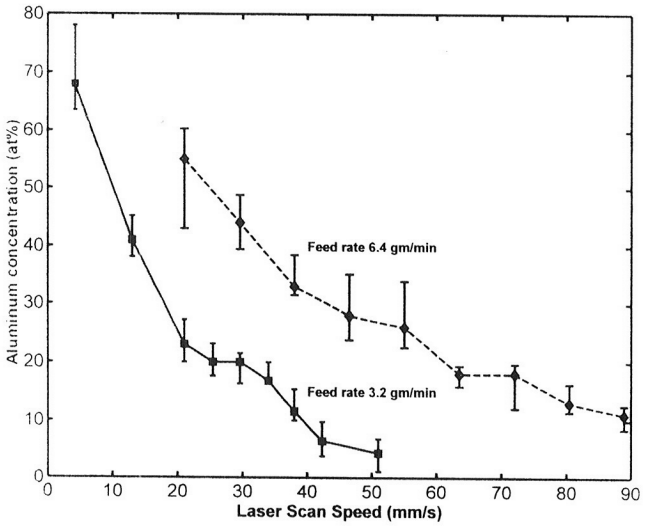


(*b*)

Fig. 2—(*a*) Plots showing the changes in aluminum concentration with depth of alloyed pools for three different scan speeds at the powder feed rate of 3.2 gm/min. (*b*) The composition plot of the aluminum concentration (at pct) *vs* various laser scan speeds at two different feed rates *viz.* 3.2 and 6.4 g/min.

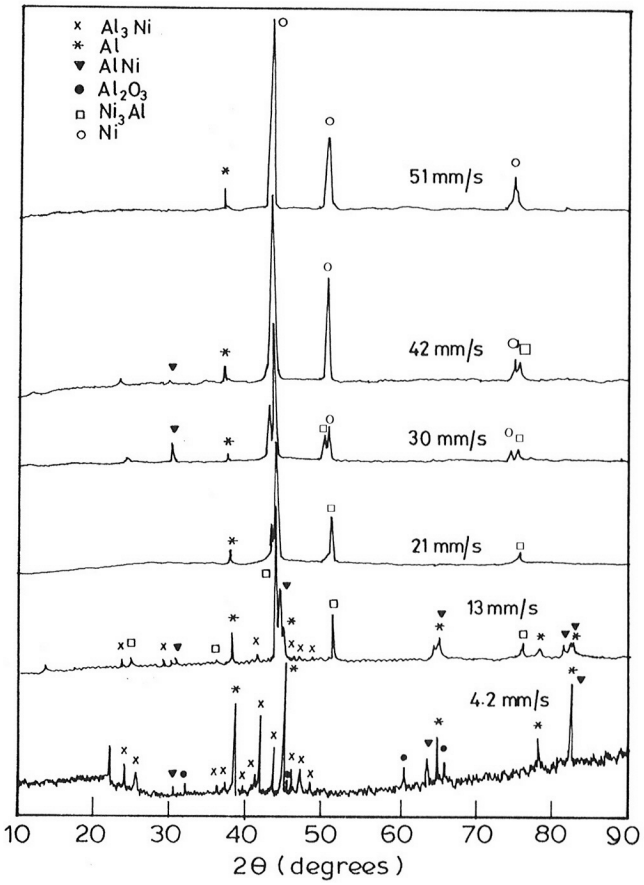


Fig. 3—X-ray diffractograms of the laser-alloyed pool at different laser scan speeds.

2. *Surface alloying at a scan rate of 13 mm/s (average composition $Al_{40}Ni_{60}$)*

The total depth of the surface alloyed region is 600 $\mu$m under this processing condition. There exists an aluminum-enriched layer at the top. The microstructure of this region shows regular rod eutectic with the occasional presence of a primary dendrite (Figure 6(a)). The selected area electron diffraction patterns from the dendrites indicate that these are $\alpha$-Al (inset). The eutectic rods are shown in detail in Figure 6(b). Microdiffraction from the rods (shown in the inset) establishes them to be $Al_3Ni$. A dark-field TEM image using the $Al_3Ni$ reflection illuminates the rods (inset of Figure 6(b)). The continuous phase in the interdendritic eutectic is $\alpha$-Al as confirmed by microdiffraction (not shown). In the remainder of the pool, we observe the AlNi B2 phase. Figure 7 shows electron diffraction patterns arranged in a unit stereographic triangle from the B2 regions. In addition to strong B2 reflections, one can observe additional weaker reflections. All these reflections can be indexed in terms of a metastable $Ni_2Al$ phase having hexagonal structure ($a$ = 0.41 nm, $c$ = 0.50 nm). This phase is closely related to what is known as ordered $\omega$ phase with $B8_2$ structure. The inset shows a dark-field micrograph illuminating this phase in an AlNi (B2) matrix.

3. *Surface alloying at a scan rate of 21 mm/s (average composition $Ni_{78}Al_{22}$)*

The entire surface-alloyed pool exhibits a two-phase microstructure consisting of primary faceted $Ni_3Al$ dendrites with interdendritic space revealing the existence of plate martensites. Figure 8(a) shows a typical low-magnification transmission electron micrograph illustrating the morphology. The selected area diffraction pattern (SADP) from a dendrite showing the [100] zone of $Ni_3Al$ is presented in Figure 8(c). The pattern contains the $L1_2$ superlattice reflections. Dark-field imaging using a superlattice reflection clearly shows the ordered domain structure (Figures 8(b) and (d)). Figure 8(d) shows a secondary dendritic arm where the domains are well developed. The majority of the domain boundaries in this micrograph align along the {110} type of planes. In contrast, the domains in Figure 8(b) show mixed sizes. This micrograph is taken from a primary arm. The central portion of the dendrite shows coarser domains. Near the edges the domains are significantly finer and contain a larger amount



Reproduced with permission of the copyright owner. Further reproduction prohibited without permission.

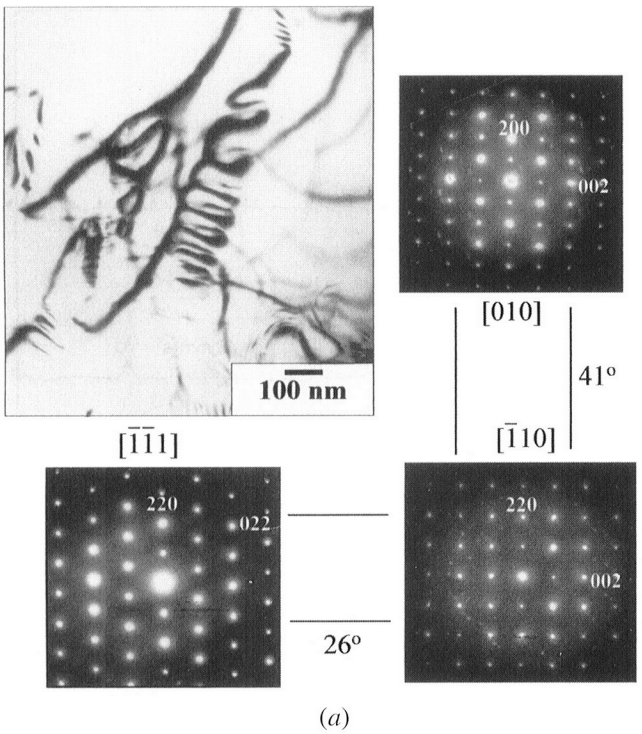


(*a*)

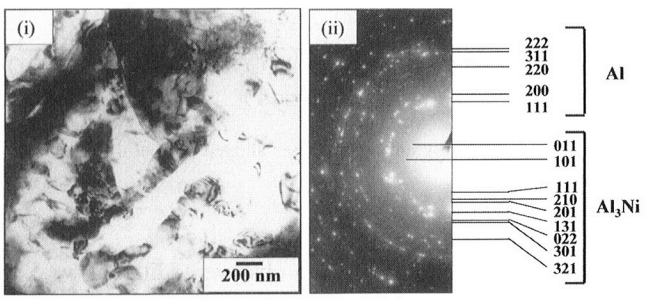


(*b*)

Fig. 4—(*a*) Bright-field TEM micrograph showing internal morphology of the $Al_3Ni$ dendrite at a distance of 1300 $\mu$m from the substrate of the laser-alloyed pool processed at 4.2 mm/s. The characteristic SADPs along important zone axes of $Al_3Ni$ on a unit stereographic triangle are presented. (*b*) (i) Bright-field TEM micrograph of the interdendritic region at a distance of 1300 $\mu$m from the substrate processed at the scan speed of 4.2 mm/s. (ii) SADP indicating the presence of both Al and $Al_3Ni$ in this region.

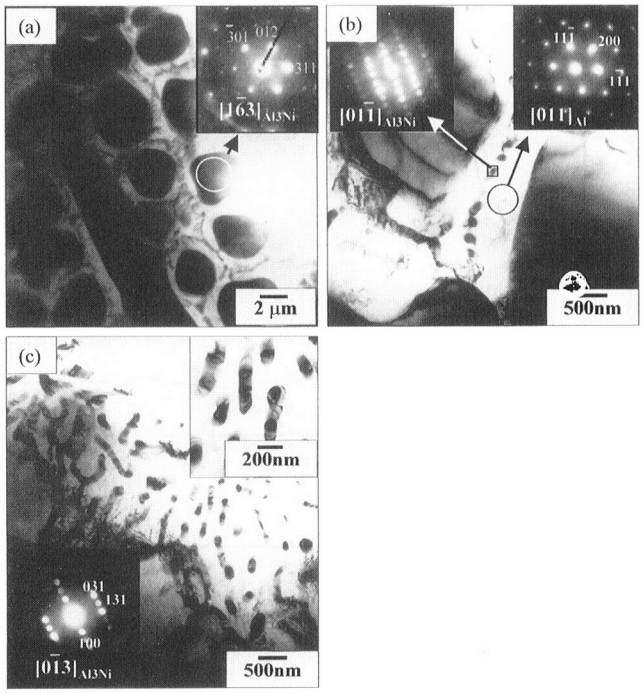


Fig. 5—(*a*) Bright-field TEM micrograph showing large $Al_3Ni$ dendrites with SADP from the dendrites shown in the inset at a distance of 900 $\mu$m from the substrate at a scan rate of 4.2 mm/s. (*b*) Higher-magnification bright-field micrograph from the interdendritic region showing Al + $Al_3Ni$ eutectic morphology. The microdiffraction from the second-phase particle is identified as $Al_3Ni$ and the SADP from the continuous phase is identified as Al. (*c*) Bright-field micrograph showing eutectic morphology at a distance of 700 $\mu$m from the substrate, and the microdiffraction pattern from one of the rods is shown in one of the insets. The higher magnification bright-field image from this eutectic morphology is shown in another inset.

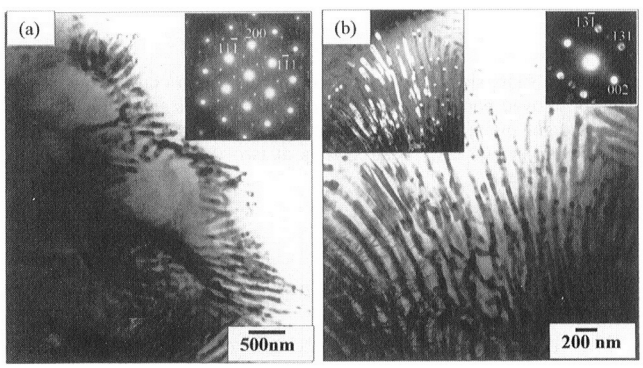


Fig. 6—(*a*) Bright-field micrograph from the top of the alloyed pool processed at a scan rate of 13 mm/s showing lamellar eutectic morphology with primary Al dendrites; the inset is the SADP from the eutectic region showing the presence of both Al and $Al_3Ni$. (*b*) Higher magnification bright-field image from the eutectic morphology. The dark-field image and the microdiffraction from one of the lamellas are shown in the inset.

of curved antiphase domain boundaries. The interdendritic spaces exhibit microstructures containing an array of martensite plates. A detailed microstructural analysis of the region is presented in Figure 9. Figure 9(a) shows a high-magnification bright-field transmission electron micrograph showing the morphologies of the martensite plates. The widths of the plates vary from 50 to 100 nm and have fine internal structures. Figures 9(b) and (c) show dark-field images of the two variants. The SADP from the composite region is shown in the inset of Figure 9(c). The microdiffraction pattern from one individual plate is shown in Figure 9(d). The pattern can be unambiguously identified as that of a 3R martensite with two twin related orientations constituting the fine internal structure of the individual lath. One can clearly see the ordered superlattice reflections in the pattern, establishing that the martensitic transformation took place from the ordered B2 matrix. The tetragonal distortion of the 3R structure becomes obvious when the sample is tilted to orient the martensitic region along the [010] direction. From the SADP along $[010]_{tetragonal}$ zone axis, as presented in Figure 9(e), the lattice



Reproduced with permission of the copyright owner. Further reproduction prohibited without permission.

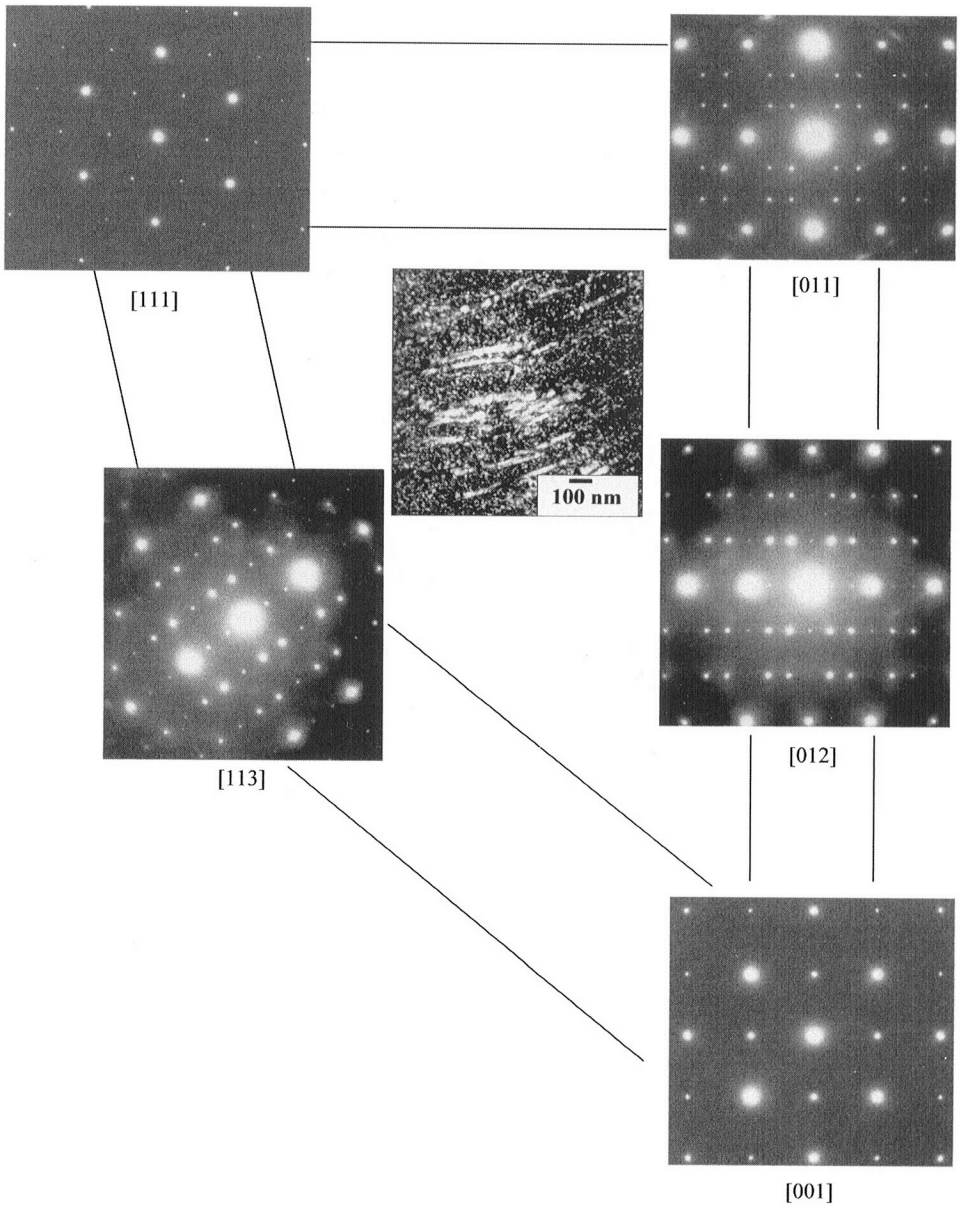


Fig. 7—Middle of the alloyed pool processed at a laser scan rate of 13 mm/s. The electron diffraction patterns along various zones arranged in a unit stereographic triangle. The brighter spots are due to the presence of B2 phase. Inset is the dark-field image formed by selecting a weak reflection with $g = 1/3$ [112] showing ordered $\omega$ type $Ni_2Al$ precipitates within B2 grain.

parameters are found to be $a = 0.372$ nm, $c = 0.346$ nm. The streaking of the diffracted spots is due to the formation of thin martensitic plates. However, some of the plates do not exhibit the internal twinning (Figure 10(a)). Figure 10(b) shows microdiffraction pattern from such a plate along the [110] zone revealing the cubic symmetry as well as the existence of ordered 100 superlattice spots inherited during martensitic transformation. This corresponds to the $L1_2$ ordered $Ni_3Al$ phase, which has a simple cubic symmetry (due to ordering based on fcc structure).

4. *Surface alloying at a scan rate of 51 mm/s (average composition Ni92Al8)*

The microstructure of the surface-alloyed region, in this case, primarily consists of nickel-rich phase. The depth of the alloyed pool is shallow; of the order of 120 $\mu$m. Detailed TEM at different depths indicates a change in state of ordering within the primary $\gamma$ fcc phase. Figure 11 shows the microstructure of a grain 60 $\mu$m away from the substrate. The SADP in the inset reveals a disordered fcc structure. Around a depth of ~100 $\mu$m away from the substrate, one starts observing the presence of ordered $\gamma'$ phase. Figure 12(a) shows the region at this depth. The diffraction patterns from the two areas of the same grain marked by boxes are shown in Figures 12(b) and (c). While Figure 11(b) shows no evidence of superlattice reflection, these are clear in Figure 12(c). The dark field from the 100 superlattice reflection reveals very fine precipitates of nanometric dimensions (Figure 12(d)), proving that the precipitates are ordered $\gamma'$ phase. The regions near the top of the alloyed pool contain ordered $\gamma'$ phase. A complete set of SADPs along a unit stereographic triangle taken from the region in Figure 13(a) is shown in Figure 13(b). The patterns also



Reproduced with permission of the copyright owner. Further reproduction prohibited without permission.

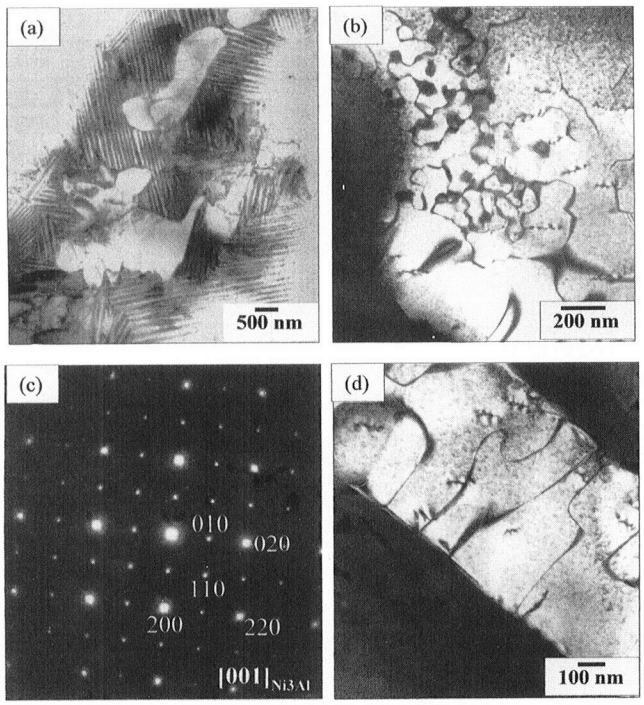


Fig. 8—(*a*) Bright-field TEM image showing the presence of dendrites and array of martensite plates in the interdendritic regions in the laser-alloyed layer processed at a scan speed of 21 mm/s. (*b*) Dark-field TEM image showing the presence of both fine and coarse ordered domains within a primary dendrite arm. (*c*) SADP along [001] zone axis from one of the $Ni_3Al$ dendrites. (*d*) Dark-field TEM image showing the presence of faceted ordered domains in a secondary dendrite arm.

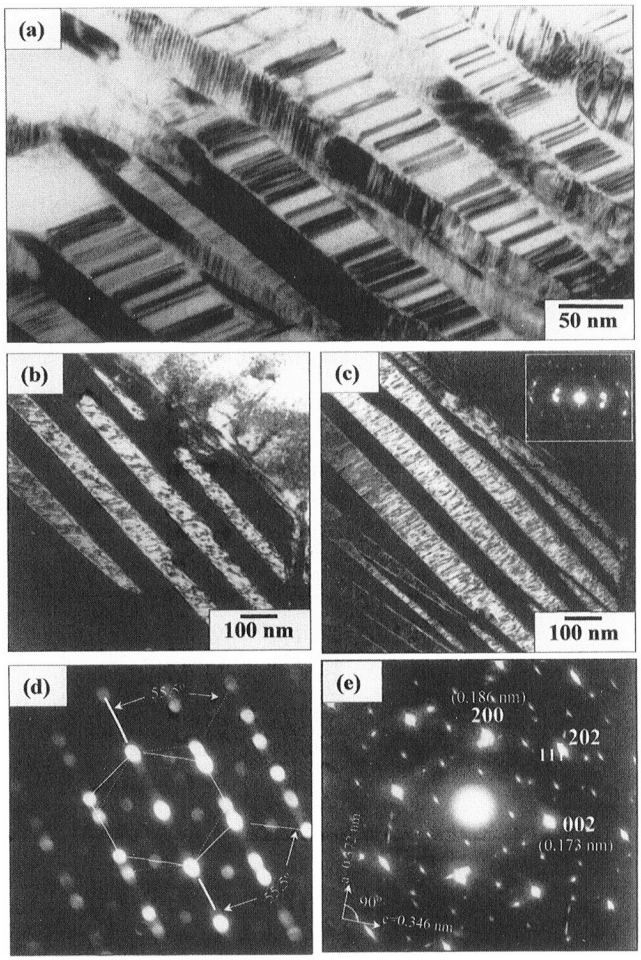


Fig. 9—(*a*) Higher magnification bright-field TEM image showing the morphology of martensite formed at a scan rate of 21 mm/s. (*b*) and (*c*) Dark-field images show the presence of two variants of martensite both exhibiting fine internally twinned morphology. The SADP from the composite region given in the inset shows the diffraction evidence of two twin variants. (*d*) The microdiffraction pattern from one of the laths of (b) shows the presence of two variants of imperfect 3R martensite within the internal fine twinned morphology. Both the variants are oriented along the [011] zone axis and twinned on the 111 plane. The angle between 100 and 111 planes is found to be 55.5 deg. (*e*) SAD pattern along [010] of tetragonal martensite showing tetragonality ($a$ = 0.372 nm, $c$ = 0.346 nm).

contain weak reflections of NiO indicating some amount of oxidation that occurred either during laser processing or sample preparation. The ordered domains, however, are still very fine, as can be seen from the inset of Figure 13(a).

## IV. DISCUSSION

The Al-Ni system contains a series of intermetallic phases starting with $Al_3Ni$ in the aluminum-rich side having an orthorhombic crystal structure. This phase forms a eutectic with $\alpha$ aluminum. The $Al_3Ni$ phase itself is a peritectic product of a reaction between liquid and the phase $Al_3Ni_2$ under equilibrium conditions. The $Al_3Ni_2$ in turn forms as a result of yet another peritectic reaction between AlNi and liquid. AlNi ($\beta$ phase) forms directly from the liquid and exists in a wide composition range around the equiatomic composition. It has an ordered B2 structure and remains ordered up to the melting point (1680 °C). The nickel-rich end is marked by $\gamma$Ni having an fcc structure containing aluminum as solute in Ni solid solution. There are some debates on the possible origin of $\gamma'Ni_3Al$, which has $L1_2$ ordering of Al and Ni atoms on the basic fcc structure. The current thinking is that it forms by a peritectic reaction between $\gamma$ and liquid under the equilibrium condition.[7] The $\beta$AlNi phase can coexist with $\gamma'Ni_3Al$ and forms a $\gamma'$-$\beta$ eutectic. However, there is evidence that a metastable eutectic reaction is possible between fcc $\gamma$ phase and $\beta$AlNi.[7] The undercooling required for this reaction is very small. At lower temperature a peritectoid reaction can

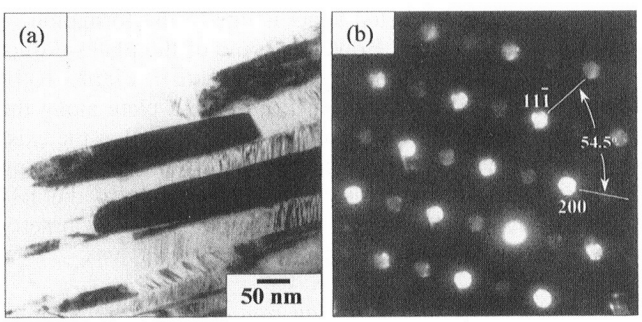


Fig. 10—(*a*) Bright-field image shows the presence of fcc martensite in between 3R. (*b*) Microdiffraction pattern from the perfect 3R martensite plate. The angle between the 100 and 111 planes is found to be 54.5 deg.



Reproduced with permission of the copyright owner. Further reproduction prohibited without permission.

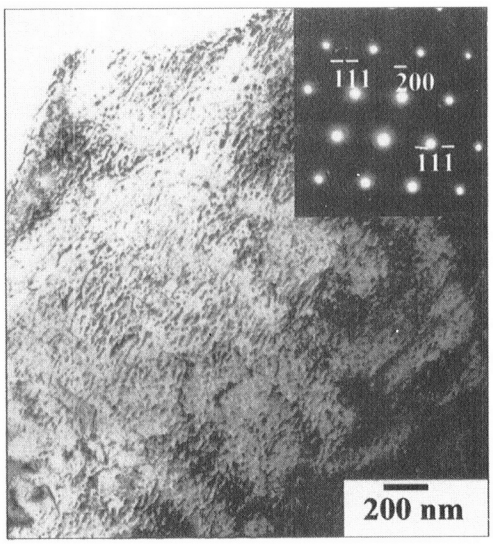


Fig. 11—The bright-field TEM image of the alloyed layer processed with a scan speed of 51 mm/s at a distance of 60 $\mu$m from the substrate. The SADP from the region shown in the inset was taken along the $[110]_{fcc}$ zone axis.

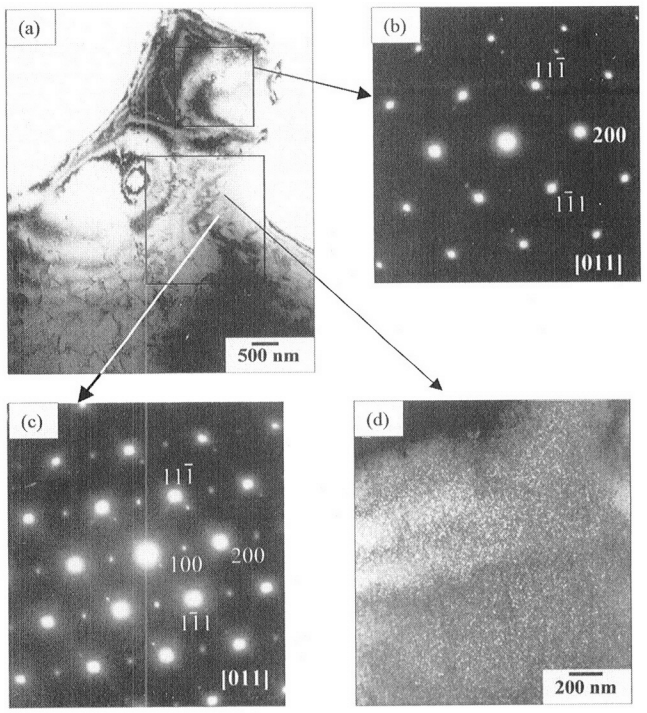


Fig. 12—(*a*) The bright-field TEM image at a distance of 100 $\mu$m from the substrate processed at a scan speed of 51 mm/s. (*b*) and (*c*) The SADPs from two different parts of the same grain marked in (a) showing the [011] zone axes of fcc and $L1_2$, respectively. (*d*) The dark-field image from the 100 superlattice spot in (c) showing the presence of ultrafine nanometer size ordered precipitates.

occur between AlNi and $Ni_3Al$ yielding another aluminide $Al_3Ni_5$. With this background information, we shall now attempt to rationalize the results of the structural and microstructural evolution in the laser-alloyed pools of Ni-Al alloys on the nickel substrate. Our results given previously also suggest a significant effect of solid-state cooling on the final microstructure, particularly in the nickel-rich compositions. An idea of the thermal history and an estimate of the cooling rate experienced by the pool during the passage of the laser, therefore, are necessary for the understanding of the evolution of the microstructure. We have arrived at an order of magnitude estimate by carrying out a simulation procedure with simplified assumptions. In Section A, we first describe briefly the results of this simulation. This will be followed by a detailed discussion of the microstructure evolution of the alloyed pools of different compositions obtained in our experiments.

### A. *A simplified estimate of the thermal history of the alloyed pool*

In order to obtain an estimate of the thermal history of the alloy pool, we have carried out a simulation using the finite difference technique. The details of the scheme are given elsewhere.[18] The model addresses melting, alloying, and subsequent cooling taking into account the fluid flow in the molten pool. Both thermal and solutal marangoni flows in the melt, which are significant in the case of laser processing, have been considered. The model does not assume any undercooling at the solid liquid interface and the solidification takes place at the temperature determined by the liquidus temperature of the alloy. The model parameters are fine tuned for the case of the alloy pool obtained at laser scanning velocity of 51 mm/s. Subsequently the same parameters were used for the other cases consistent with the experimental practice. Figures 14(a) and (b) give the temperature profiles for two scanning speeds of 21 and 51 mm/s along the scan direction, at a constant feed rate of 3.2 g/s. The bold line gives the interface between solid and liquid. One can clearly see the trailing of the molten melt pool for the high scanning rate. Typical temperature histories of the center of the pool at scan rates of 21 and 51 mm/s are shown in Figure 14(c). The slope of this curve gives the cooling rate at different times. Trailing of the melt pool has a strong influence on the solid-state cooling. Typical cooling rates as a function of time in the solid state for the two scan speeds are shown in Figure 14(d). The cooling rate is significant even in the solid state and is of the order of $10^4$ K/s.

### B. *Microstructure Evolution in the Laser-Alloyed Pool*

#### 1. *Aluminum-rich alloy surfaces*

The surface-alloyed layers processed with laser at low scan rates yield aluminum-rich compositions. The microstructure predominantly contains the $Al_3Ni$ intermetallic phase. Composition analyses of these alloyed pools show comparatively larger scatter. For example, the sample processed with a scan velocity of 4.2 mm/s and feed rate of 3.2 g/s gives analyzed composition varying from 65 to 78 at. pct Al. At these compositions, the orthorhombic $Al_3Ni$ phase is expected to be the predominant phase. Our TEM observations reveal the primary dendrites to be $Al_3Ni$, indicating that this is the first phase to form in the alloyed pool. The interdendritic spaces contain eutectic of $\alpha$ Al and $Al_3Ni$. Near the top of the clad layer, the two phases coexist in fine-equiaxed form. The coupled eutectic is more developed and has a rod eutectic morphology with increasing volume fraction toward the substrate-melt interface. These results suggest that a significant amount of aluminum has traveled toward the



Reproduced with permission of the copyright owner. Further reproduction prohibited without permission.

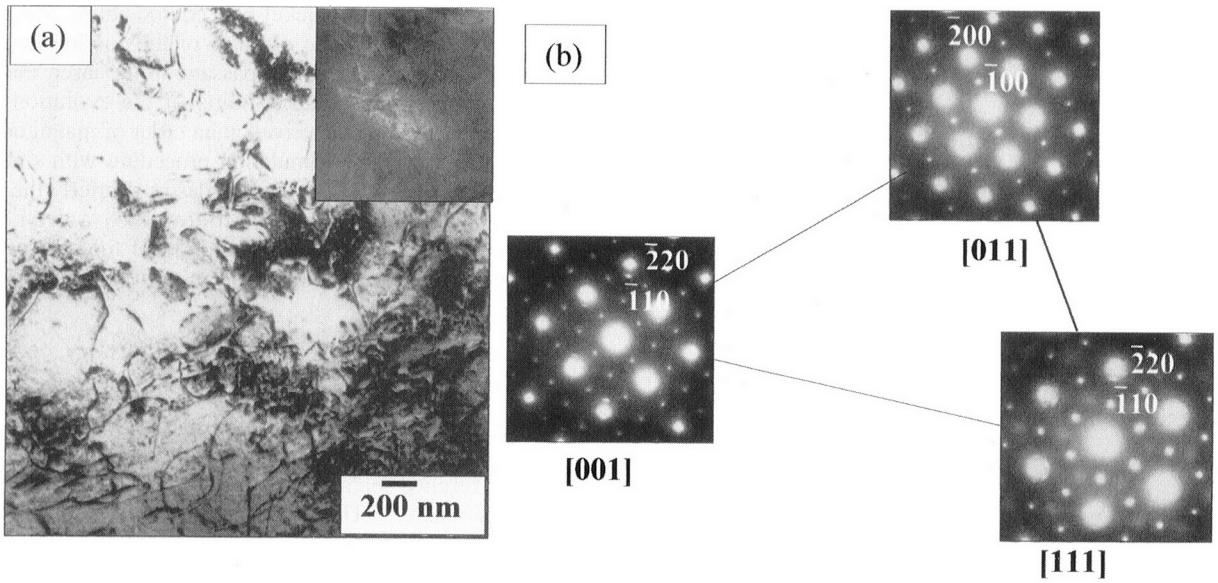


Fig. 13—(*a*) Bright-field TEM micrograph and corresponding 100 superlattice dark-field image in inset showing fine domains of $L1_2$ at the top of the laser-alloyed pool processed at a scan rate of 51 mm/s. (*b*) SAD patterns along [001], [011], and [111] zone axes of $L1_2$ arranged in a unit stereographic triangle show the characteristic superlattice reflections due to $L1_2$ ordering.

bottom due to the domination of the surface-induced flow in the weld pool. This is expected from our simulation results. The observed microstructure is also consistent with the expected growth scenario. The regions just below the surface need to grow at higher velocities to keep the steady-state solid-liquid interface profile. The growth rate will be smaller toward the substrate. Under this condition, there are two choices for the melt near the top. Either the solid phases grow at higher speed dictated by the scan velocity or there is an increase in the undercooling of the melt so that a higher rate of nucleation of the phases maintains the requirement of fraction solidified for a steady-state solidification front near the top layer. Our results suggest that near the top surface, coupled growth of the eutectic in the interdendritic space breaks down and the evolution of the two phases occurs by a nucleation-controlled mechanism. This is evidenced in the microstructure, which shows the presence of small $Al_3Ni$ grains embedded in the continuous $\alpha$ Al matrix. This suggests that the liquid in the interdedritic region has undercooled significantly. It can be noted that no orientation relation between the $\alpha$ Al and $Al_3Ni$ could be found in the eutectic regions, neither near the top nor near the substrate.

2. *The nickel-rich surface alloys*

The situation changes dramatically as we increase the scan rate. Even at a scan rate of 13 mm/s (feed rate 3.2 g/s), we have obtained a nickel-rich surface alloyed layer with average composition of $Al_{40}Ni_{60}$. Under equilibrium situations, this corresponds to a two-phase region consisting of B2 AlNi and the intermetallic $Al_3Ni_5$. The latter forms by a peritectoid reaction between $Ni_3Al$ and AlNi. This reaction is completely suppressed during laser surface alloying, because the cooling rate at solid state is fairly rapid. This is discussed in Section A. Our experimental results indicate an aluminum-rich region at the top surface, which consists of regular $\alpha$ Al-$Al_3Ni$ eutectic, together with the primary $\alpha$ Al. This suggests that due to a large difference in melting points, some amount of aluminum may be melting at the surface, while solidification is in progress in the interior creating a thin aluminum-rich surface layer. However, if we ignore this layer, the microstructure is uniform at different depths of the alloyed pool and consists of a matrix phase containing uniform dispersion of a precipitate phase. As presented in Section III, the matrix has an ordered B2 structure and the precipitates can be identified as $Ni_2Al$, which has the structure type $B8_2$ having hexagonal symmetry. This was earlier reported during long-term aging of Ni-Al alloys.[9,10,11] The $B8_2$ structure can be viewed as ordered $\omega$ structure with the *c*-axis of the ordered $\omega$ structure twice that of the disordered $\omega$ structure. The superlattice reflections due to $B8_2$ ordering can be easily detected in the SAD patterns corresponding to the $[111]_\beta$ zone. In this zone, the allowed $\omega$ reflections coincide with the $\beta$ reflections and the superlattice reflections due to $B8_2$ ordering appear as extra reflections. For example, the $1/3(112)_\beta$ reflections due to $B8_2$ ordering correspond to $\{10\bar{1}0\}$ planes of chemically disordered $\omega$. The structure factor of this set of planes in chemically disordered $\omega$ structure is zero. Thus, the appearance of these additional reflections in this zone indicates chemical ordering. The ordered $\omega$ structure clearly represents a situation where both the displacement ordering and replacement ordering have taken place simultaneously.[12] The rapid solidification and hence incorporation of excess vacancies may have a role in the process of the formation of $\omega$ phase. The collapse of these vacancies (known as "$\omega$-collapse") can result in the formation of this structure from the chemically ordered B2 structure.[9]

The samples alloyed with laser scan velocities of 21 mm/s yield complex pathways for microstructural evolution. The alloy pool has an average composition of $Ni_{78}Al_{22}$. However, the composition analysis reveals some amount of scatter. It has been recently shown with undercooling experiments that the microstructural pathways in this region depend sensitively on the composition.[13] Remarkably, we have not



Reproduced with permission of the copyright owner. Further reproduction prohibited without permission.

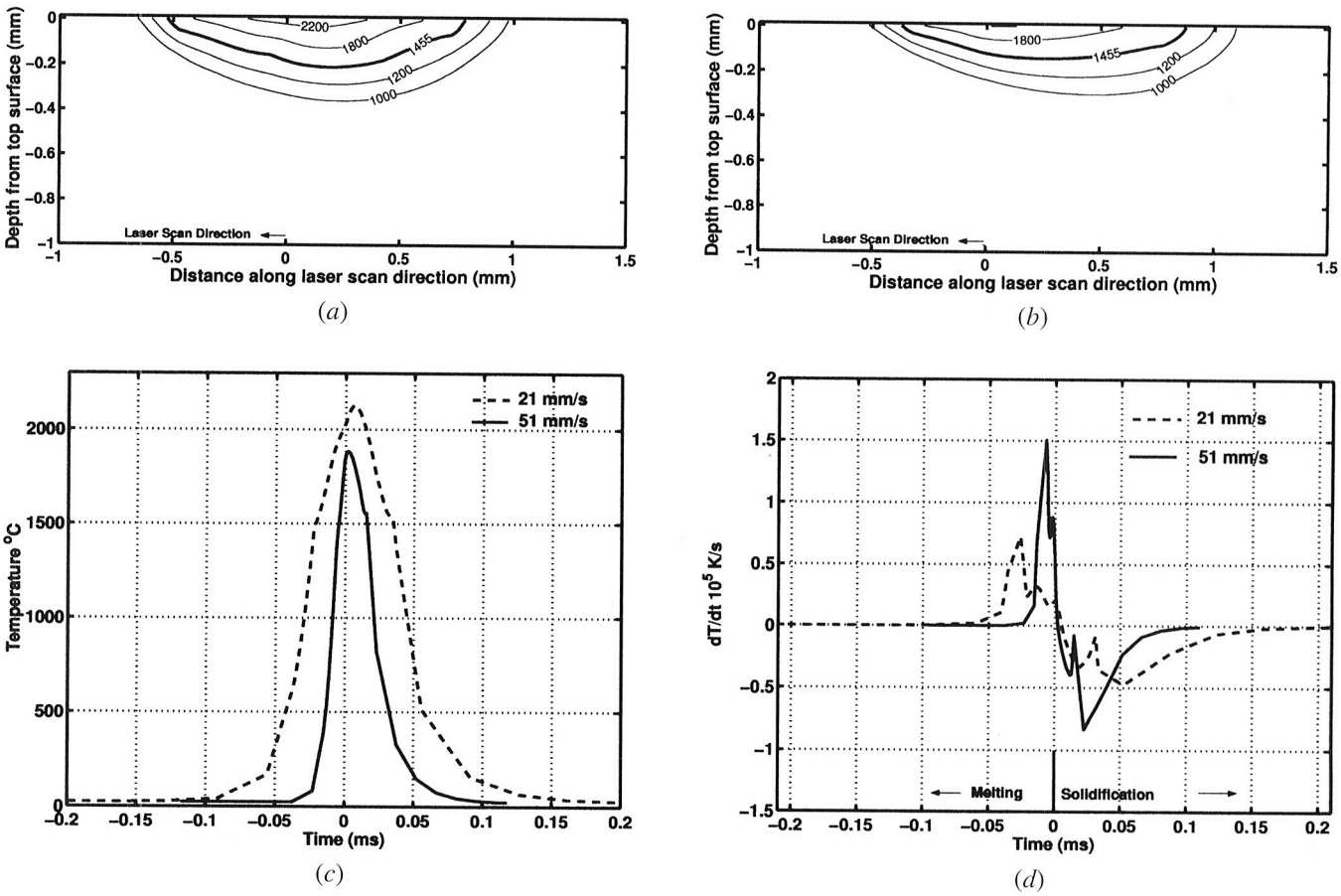


Fig. 14—Computed temperature profiles across and along the laser scan direction for two scanning speeds of (*a*) 21 mm/s and (*b*) 51 mm/s. (*c*) Thermal history at the center of clad pool. (*d*) Cooling rates with time for scan speeds 21 and 51 mm/s.

observed a significant difference in the microstructure across the laser-alloyed pool. The microstructure consists of dendrites of ordered $\gamma'$ and martensite with 3R structure in the interdendritic regions. Only the proportion of the martensite and the primary dendrite differs from region to region. According to the work of Hunziker and Kurz,[14] for our growth rates and composition, one expects cellular microstructure of $\gamma$ phase.

The superlattice dark-field imaging of the $\gamma'$ dendrites reveals fine-ordered domain structure, with domain size varying from the side to the center of the dendrite. As discussed by Cahn *et al.*,[15] such domain morphology clearly reflects reordering in the solid state and provides evidence for the formation of disordered phase during solidification. Clearly, the undercooling achieved in the melt is large enough for the melt to enter into the $\gamma'$ phase field of the equilibrium diagram. The $\gamma'$ phase forms in the equilibrium diagram by a peritectic reaction. This is clearly suppressed during laser processing. Although the $\gamma'$ phase in principle can nucleate from liquid, our observation of fine domain structure suggests the formation of metastable $\gamma$ dendrites. The $\gamma$ phase reorders in solid state during cooling subsequent to solidification. The nature of phase evolution can be anticipated by an analysis of the metastable phase diagram. Such a diagram is calculated by Assadi *et al.*[13] However, in the present case, simple extensions of the $\gamma$, $\gamma'$, and $\beta$ liquidus boundaries are sufficient to rationalize our observation. This is shown schematically in Figure 15. Two possible pathways for the formation of disordered $\gamma$ can be envisaged. There exists growth competition between $\gamma'$ and $\gamma$ phases when the liquid is undercooled below both the extended $\gamma'$ and $\gamma$ liquidus lines. This has been estimated by Assadi *et al.*[13] and observed in the thin films of $Ni_{75}Al_{25}$ processed with 300 ns pulse laser.[16] According to the estimate of Assadi *et al.*, below a critical undercooling, metastable $\gamma$ grows faster than $\gamma'$ phase. The second possibility is the nucleation of $\gamma'$ phase, which, during rapid growth undergoes disorder trapping. However, the latter route is less likely since nucleation of disordered $\gamma$ is more likely than ordered $\gamma'$ in a process dominated by random fluctuations. The $\gamma$ formed by the first route can also undergo solute trapping at very high growth velocity, thereby increasing the driving force for reordering at lower temperature.

In case the trapping is partial, the solute partitioning will take place with the new metastable liquidus following a path parallel to the extrapolated $\gamma$ liquidus in between the liquidus and the $T_0^\gamma$ line. The extrapolated liquidus will always be below the $\beta$ liquidus and the undercooled melt ahead of the dendrite will experience a driving force for the liquid to $\beta$ AlNi transformation. For the case of the metastable liquidus for partial solute trapping, this is true beyond the composition for the intersection of the extrapolated $\gamma$ liquidus with the extrapolated $\beta$ liquidus. The compositions beyond the intersection of this line with the $T_0^\beta$ will indicate driving



Reproduced with permission of the copyright owner. Further reproduction prohibited without permission.

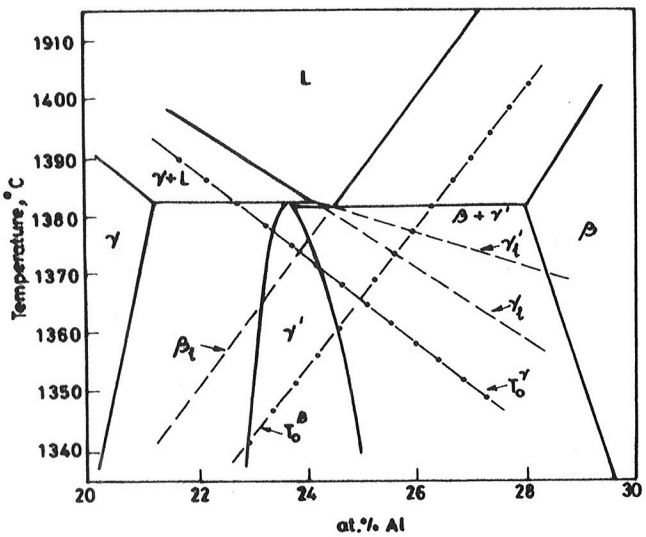


Fig. 15—Part of the Ni-Al phase diagram showing metastable extensions of $\beta$, $\gamma$, and $\gamma'$ liquidus lines marked as $\beta_l$, $\gamma_l$, and $\gamma_l'$, respectively. The lines marked as $T_o^\gamma$ and $T_o^\beta$ are $T_o$ lines of the respective phases.

force for the diffusionless solidification. Thus, depending on the amount of undercooling and the location of the $T_o$ curve for the $\beta$ phase, a diffusionless transformation can occur since the time for partitioning during solidification is limited. As shown earlier, the cooling rate in the solid state is fairly rapid. This promotes martensitic transformation of the as-solidified ordered B2 phase.

The observation of the 3R martensite is consistent with that of the earlier investigators who reported the composition of 63 at. pct for a change over from monoclinic 7M martensite to 3R martensite.[17,18] These martensites exhibit microtwinning[19] and have an fct ($L1_0$) structure. It occurs over a range of composition around $Ni_{65}Al_{35}$ with excess Ni in the ordered structure randomly distributed in the sublattice.[20] The $c$ parameter is generally smaller than the $a$ parameter. It is shown that the $c/a$ ratio depends sensitively on composition and increases with increasing Ni content.[19]

The twinned martensite observed by us has tetragonal distortion. The lattice parameters observed in our samples are $a = 0.372$ nm and $c = 0.346$ nm. The observed $c/a$ is 0.978, which can be compared with the $c/a$ of 0.87 observed in the case of martensite obtained by water quenching of $Ni_{66}Al_{34}$ alloy.[21] The $c/a$ is significantly larger than that observed by earlier investigators. While the value of the $a$ parameter is smaller, the $c$ parameter is larger than that obtained by solid-state quenched martensite. The twinning operation in the 3R martensite accommodates the inhomogeneous deformation. Clearly, unlike the earlier observations, the microstructure evolution in our laser-alloyed pool is the result of the competition between the dendritic growth of supersaturated disordered $\gamma$ and massive growth of ordered $\beta$, followed by the martensitic transformation of the $\beta$ phase. We have occasionally observed plates exhibiting no internal structure (Figure 10). These have perfect 3R structure with very little tetragonal distortion. The faint superlattice spots suggest a $L1_0$ ordering with a very low order parameter. Alternately, these may be ordered $\gamma'$ phase, which may have formed along with the B2 NiAl during solidification. A better understanding is needed to explain the origin of these plates.

The microstructure of alloy pool processed at a laser scan velocity of 51 mm/s clearly suggests the existence of a composition gradient with the top layer richer in aluminum. Thus, the disorder near the substrate gives way to order toward the top. However, the fine nanometer size precipitates of ordered phase $\gamma'$ within the disordered phase $\gamma$ again reveal that the primary solidification product is $\gamma$ phase. This phase is shown to order partially in the solid state depending on local composition. This can happen even in different locations of the same grain reflecting local inhomogeneities of the melt composition inherited by the growing solid.

## V. CONCLUSIONS

Detailed TEM studies were carried out on clad layers produced by different scan speeds and powder feed rates. The evolution of the various solidification microstructures seems to be dictated primarily by the chemical composition and its variation within the various layers, which in turn are dependent on laser scan speed and powder feed rates. The compositional analysis, TEM results, and simulation results support each other. High quenching rates involved during the development of solidification microstructures leads to the formation of various metastable phases and ultrafine nanometer scale microstructures. The important observations are as follows:

1. precipitation of ordered $\omega$ structured $Ni_2Al$ within B2 grains;
2. formation of disordered $\gamma$, which reorders to yield $\gamma'$ $Ni_3Al$;
3. transformation of B2 phase into 3R martensite plates coexisting with those of $\gamma'$-$Ni_3Al$; and
4. development of fine nanometer scale ordered domains in the Al-rich part of primarily solidified $\gamma$Ni solid solution within the same grain.

## ACKNOWLEDGMENTS

The authors acknowledge the financial support from the Council of Scientific and Industrial Research, India, and United States Office of Naval Research.

## REFERENCES

1. J.A. Folkes: *Surface Coatings Technol.*, 1994, vol. 63, pp. 65-71.
2. J.I. Nurminen and J.E. Smith: *Proc. Conf. on Applications of Lasers in Materials Processing*, E.A. Metzbower, ed., ASM, Metals Park, OH, 1970, p. 94.
3. T. Chande and J. Majumder: *Proc. Conf. on Applications of Lasers in Materials Processing*, E.A. Metzbower, ed., ASM, Metals Park, OH, 1970, p. 127.
4. L. Renaud, F. Fouquet, A. Elhamdaoui, J.P. Millet, H. Mazille, and J.L. Crolet: *Acta Metall.*, 1990, vol. 38, pp. 1547-53.
5. G.K. Dey, U.D. Kulkarni, I.S. Batra, and S. Banerjee: *Acta Metall. Mater.*, 1994, vol. 42, pp. 2973-81.



Reproduced with permission of the copyright owner. Further reproduction prohibited without permission.

6. J.H. Abboud, R.D. Rawlings, and D.R.F. West: *J. Mater. Sci.*, 1995, vol. 30, pp. 5931-38.
7. J.H. Lee and J.D. Verhoeven: *J. Phase Equilibria*, 1994, vol. 15, pp. 136-46.
8. P. Mohanraj, S. Sarkar, S. Chakraborty, G. Phanikumar, P. Dutta, and K. Chattopadhyay: *Int. J. Heat Fluid Flow*, 2002, vol. 23, pp. 298-307.
9. P. Georgopoulos and J.B. Cohen: *Acta Metall.*, 1981, vol. 29, pp. 1535-51.
10. P.F. Reynaud: *Scripta Metall.*, 1977, vol. 11, pp. 765-70.
11. P.F. Reynaud: *J. Appl. Cryst.*, 1976, vol. 9, pp. 263-68.
12. S. Banerjee and R.W. Cahn: *Acta Metall.*, 1983, vol. 31, pp. 1721-35.
13. H. Assadi, M. Barth, A.L. Greer, and D.M. Herlach: *Acta Mater.*, 1998, vol. 46, pp. 491-500.
14. O. Hunziker and W. Kurz: *Acta Mater.*, 1997, vol. 45, pp. 4981-92.
15. R.W. Cahn, P.A. Siemers and E.L. Hall: *Acta Metall.*, 1987, vol. 35, pp. 2753-64.
16. O. Bostanjoglo and V. Penschke: *J. Appl. Phys.*, 1993, vol. 72, p. 8201.
17. Y.K. Au and M. Wayman: *Scripta Metall.*, 1972, vol. 6, pp. 1209-14.
18. S. Muto and D. Schryvers: *J. Alloys. Compounds*, 1993, vol. 199, pp. 1-6.
19. D. Schryvers, B. DeSagher, and J. van Landuyt: *Mater. Res. Bull.*, 1991, vol. 26, pp. 57-66.
20. K. Enami, S. Nenno, and K. Shimizu: *Trans. Jpn. Inst. Met.*, 1973, vol. 14, pp. 161-65
21. D. Schryvers: *Phil. Mag. A*, 1996, vol. 68, pp. 1017-32



Reproduced with permission of the copyright owner. Further reproduction prohibited without permission.